



OPEN

Dispersion of metallic/ceramic matrix nanocomposite material through porous surfaces in magnetized hybrid nanofluids flow with shape and size effects

M. Zubair Akbar Qureshi¹✉, S. Bilal², M. Y. Malik³, Qadeer Raza¹, El-Sayed M. Sherif^{4,5} & Yong-Min Li⁶✉

Matrix nanocomposites are high performance materials possessing unusual features along with unique design possibilities. Due to extraordinary thermophysical characteristic contained by these matrix nanocomposites materials they are useful in several areas ranging from packaging to biomedical applications. Being an environment friendly, utilization of nanocomposites offer new technological opportunities for several sectors of aerospace, automotive, electronics and biotechnology. In this regards, current pagination is devoted to analyze thermal features of viscous fluid flow between orthogonally rotating disks with inclusion of metallic matrix nanocomposite (MMNC) and ceramic matrix nanocomposites (CMNC) materials. Morphological aspects of these nanomaterials on flow and heat transfer characteristics has been investigated on hybrid viscous fluid flow. Mathematical structuring of problem along with empirical relations for nanocomposites materials are formulated in the form of partial differential equations and later on converted into ordinary differential expressions by using suitable variables. Solution of constructed coupled differential system is found by collaboration of Runge–Kutta and shooting methods. Variation in skin friction coefficient at lower and upper walls of disks along with measurement about heat transfer rate are calculated against governing physical parameters. Impact of flow concerning variables on axial, radial components of velocity and temperature distribution are also evaluated. Contour plots are also drawn to explore heat and thermal profiles. Comparison and critical analysis of MMNC and CMNC have been presented at lower and upper porous disks. Our computed analysis indicates that hybrid nanofluids show significant influence as compared to simple nanofluids with the permutation of the different shape factors.

Abbreviations

B_o	Uniform magnetic field (T)
C_f	The total skin friction coefficient
C_p	Specific heat at constant pressure
k	Time depended on coefficient
M	Magnetic parameter
P_r	Prandtl number
$r z$	Cylindrical coordinates system
R	Reynolds number
W	Mass or velocity component along z-axis

¹Department of Mathematics, Air University Islamabad, Multan 60000, Pakistan. ²Department of Mathematics, P.A. F Complex, Sector E-9, Air University, Islamabad 44000, Pakistan. ³Department of Mathematics, College of Sciences, King Khalid University, Abha 61413, Kingdom of Saudi Arabia. ⁴Research Chair for Tribology, Surface, and Interface Sciences (TSIS), Department of Physics and Astronomy, College of Science, King Saud University, P.O. Box 2455, Riyadh 11451, Saudi Arabia. ⁵Center of Excellence for Research in Engineering Materials (CEREM), King Saud University, P.O. Box 800, Riyadh 11421, Saudi Arabia. ⁶Department of Mathematics, Huzhou University, Huzhou 313000, People's Republic of China. ✉email: drzubairzero@gmail.com; ymlwww@163.com

Nu	Nusselt number
ρ_{hmf}	Density for (HN_{fd})
ρ_{s2}	Density for second solid NP's
k_{s1}	Thermal conductivity for first solid fraction
k_{mbf}	Thermal conductivity for shape base fluid
k_{bf}	Thermal conductivity for base fluid
μ_{bf}	Viscosity based fluid
ν_{hmf}	Kinematics viscosity for (HN_{fd})
F_η	The dimensionless radial velocity profile
θ_η	Dimensionless temperature profile
σ	Electrical conductivity ($(m^3 A^2)/kg$)
ν	Kinematic viscosity (m^2/s)
μ	Dynamic viscosity (Pa s)
ρ	Density (kg/m^3)
ρC_p	Volumetric heat capacity ($J/(m^3 K)$)
$T (HN_{fd})$	Temperature (K)
A_1	Dimensionless parameter coefficient
$(\rho c_p)_{hmf}$	Specific heat capacity for (HN_{fd})
ρ_{s1}	Density for first solid NP's
k_{hmf}	Thermal conductivity for (HN_{fd})
k_{s2}	Thermal conductivity for second solid fraction
P	Pressure
μ_{eff}	Viscosity for effect
dp	Dimeter of particles
Nu_z	Nusselt number

Subscripts

(B_{fd})	Base fluid
(HN_{fd})	Hybrid Nanofluid
(N_{fd})	Nanofluid
HNF1	($Fe_3O_4 - TiO_2/H_2O$)
HNF2	($Fe_3O_4 - Al_2O_3/H_2O$)
HNF3	($Al_2O_3 - TiO_2/H_2O$)
HNF4	($TiO_2 - Cu/H_2O$)
1	First nanoparticle (Fe_3O_4)
2	Second nanoparticle (Al_2O_3)
3	Third nanoparticle (TiO_2)
4	Forth nanoparticles (Cu)

Greek symbols

α	Thermal diffusivity (m^2/s)
φ	Equivalent nanoparticles volume fraction
φ_1	Equivalent first nanoparticles volume fraction
η	Independent similarity variable
φ_2	Equivalent first nanoparticles volume fraction

With advancement in technology modern thermal management systems like central processing units in computers, light emitting diodes, transistor, solar collectors, audio amplifiers and so forth requires liquids with improved thermal conductivity. Since, ordinary fluids are unable to meet desired requirements for advanced industrial and technological procedures so insertion of nanoparticles in poorly conducting ordinary liquids are managed. The appropriate mixture of nanoparticles in specified ratios has generated exceptional thermal performance of weak thermalized systems. The concept of addition of nanoparticles was inaugurated by Choi and Eastman¹ which laid the basis of nanotechnology. Initially, nanofluids are considered as single phase flows but it is experimentally proved that consideration of nanoliquid as two phase compositions is much more beneficial. Yamada et al.² discussed the combined two or more than two organic and inorganic constituents at nanoscale which are obliged in polymers. This idea executed hybridization of nanoparticles with different organic/inorganic compositions. The hybridization of base fluid with multiply structured nanoparticles change dynamics of industrial world³.

From advent of twenty-first century a new findings in nanotechnology is discovered which is the concept of matrix nanocomposites materials. It is a two phase material with one phase consisting of solid material and other phase is nanometer sized particles. Nanomaterials are lightweight, highly strength full, sustainable, elevated temperature strengthened, corrosion resisted can be used in a wide variety of applications, e.g. aerospace, automotive, biomedical engineering etc. On basis of such mechanical, electrical, thermal, optical, electrochemical and catalytic features nanocomposites are characterized in to ceramic/metal matrix nanocomposites. MMNC is the material which composes of metal matrix distributed in concrete, ceramic, or organic substances. The reinforcement and distribution of matrix material into nano-scale particles which generates remarkable improvement in mechanical properties of formed composition. In metal matrix composites metals like copper, magnesium, and aluminum are capitalized as base metal. Since, base materials are metal which have stiffness and strength so

MMNC is obliged in aviation, aerospace, defensive weapons and other areas. The most widely used reinforcements in matrix nanocomposites are Silicon Carbide (SiC), TiO₂, Aluminum Oxide (Al₂O₃) because of fact that they provide strong wear resistance and compressive power. In addition, majority volume of matrix metal composites are filled by a ceramic such as nitrides, oxides, silicides and borides. To gain optimized usage and evoking of precise nanoscopic features the ceramics as well as metallic elements are uniformly distributed. Zeeshan et al.⁴ investigated influence of morphological aspects of nanoparticles by varying shape on features of fluid floating across a spinning disk. Ahmad et al.⁵ depicted magnetized nano squeezed flow between two parallel disks along with consideration of viscous dissipation and multi natured hybrid particles. Haq et al.⁶ inserted Manganese-Zinc ferrite and Cobalt ferrite in viscous fluid flow between parallel disks and adumbrated enhancement in thermal conductance. Heat transfer features by inducting platelet, cylinder, and brick-shaped copper nanoparticles in water was studied by Khan et al.⁷ Hajabdollahi et al.⁸ examined morphometric aspects of (Al₂O₃) nanoparticles by considering platelets, spherical, cylindrical shapes, and bricks shapes on performance of tube heat exchangers. Kucharik et al.⁹ discussed absorption of metallic particles in water for formation of colloidal substances used in heat transfer diffusion processes in lasers. Ghozatloo et al.¹⁰ analyzed experimentally about dynamics of insertion of gold nanoparticles in water and ethylene glycol and build comparative framework regarding affectivity of particles against viscosity variant base liquids.

Heat is form of energy that arises due to temperature difference. Heat transfer with in flow procedures has received several applications like in electric power production, vehicle propulsion and climate control devices, home heating, and cooling appliances and so many. Heat transmits during the flow by the way of conduction, convection, and radiation. Generally, heat transfer in fluid arises due to convective motion of liquid molecules and enhanced is done by uplifting thermal conductivity of liquid. Researchers have experimentally discovered that this is executed by adding nanoparticles. This experimentation is proved to be successful when cooling and heating of domestic appliance like refrigerator, coils and electrical device is raised by nanoparticles inclusion. Chamkha et al.¹¹ investigated unsteady squeezing flow and upsurge in convective motion of fluid molecules bounded between two parallel disks. Mochizuki et al.¹² conducted experimental analysis the mount in thermal conductivity of viscous fluid flowing between two parallel heated disks rotated radially. Characteristics of hall current on hybridized nanofluid flow across spinning disk was demonstrated by Acharya et al.¹³. Bhattacharyya et al.¹⁴ examined enhancement in heat transfer properties of viscous liquid between two coaxial disks by adding carbon nanotubes. Bhat et al.¹⁵ analyzed heat transfer in flow through addition of nanostructures in a porous disk by employing tangential slip level constraint at boundary. Maskeen et al.¹⁶ established hybridized nano fluid flow with combination of alumina and copper particles under impact of Lorentz magnetic field. Ghaffar et al.¹⁷ numerically studied heat transfer in incompressible flow of fluid between two orthogonally passing coaxial porous disks with interaction of ferromagnetic nanoparticles.

In recent years some inconsistencies in reported results regarding heat transfer rate with addition of nanoparticles is found. So, researchers have tried to use hybridized nanofluid which is engineered suspension of dissimilar nanoparticles in mixture or in composite form. This idea has further improved heat transfer and pressure drop characteristics and removed disadvantages of individual suspension. With the formation of hybridized nanofluids a better thermal network containing synergistic effect of nanomaterials is attained. In this regard several studies is available in literature like Behnam et al.¹⁸ used hybridization of Titanium dioxide with Silicon Carbide in heavy water limited between moveable disks under effect of vertical magnetic field. Use of hybrid nanofluid during treatment of cancer patients was disclosed by Hayat et al.¹⁹. Enhancement in thermal transfer by using hybrid nanofluid during industrial procedures was explained by Hussein et al.²⁰. Devi et al.²¹ examined hydro-magnetic hybrid nano-liquid (Cu-Al₂O₃/water) for raise in temperature and heat transfer up gradation in liquid flowing in permeable flow domain. Sarkar et al.²² evaluated optimistic impact of hybridization of nanoparticles for enhancing temperature profile. Sundar et al.²³ provided comparative analysis regarding heat transfer features attained with addition of ordinary and hybridized nanoparticles.

Magneto hydrodynamics describe flow behavior of moving conducting liquid which in turns polarized it. Impact of magnetic field is evaluated in industrial processes like fuel industry, electric generators, nuclear plants, aerodynamics, crystal production and so forth. Tamim et al.²⁴ analyzed MHD flow and its practical appliance in multiple sectors. The field of magneto hydrodynamics was introduced by Alfven et al.²⁵. Emad et al.²⁶ demonstrated analytical and numerical treatment about hybrid magnetic nano material in porous stretching/shrinking medium. Ghadikolaei et al.²⁷ analyzed heat transfer features of electrical conducting hybridized nano liquid (TiO₂-Cu) in water by varying shape of nanoparticles. Hayat et al.²⁸ explored magnetically effected fluid flowing between two parallel spinning disks by using analytical approach. Ahmad et al.²⁹ explored impact of magnetic field on asymmetric flow of fluid and found decrease in momentum profile. Rashidi et al.³⁰ magnetic flow of viscous fluid by interpreting impact of it on thermal conductivity. Raddya et al.³¹ explored impact of magnetic field on nano-liquid flow in rotating frame and found reduction in velocity against Hartmann number. Mliki et al.³² demonstrated convective flow of nano fluid under appliance of MHD in an enclosure by examining thermo physical features. Turkyilmazoglu et al.³³ explicated heat transfer features of magnetized viscous fluid flow generated by spinning disks. Some recent literature about flow characteristics of fluid under appliance of magnetic field in different physical configurations is enclosed in³⁴⁻³⁸. Sheikholeslami et al.³⁹ aimed to investigate hot gas flow inside inner pipe and operating fluid in the annulus region filled with nanoparticles composed of CuO. Wang et al.⁴⁰ analyzed utilization of hybrid nanofluid in solar photovoltaic system using the spectral beam splitting technology. Chuanpan et al.⁴¹ described a high-efficiency sensing system working with carbon nanofibers and discussed it efficiency by varying shape and amount of fibers. Guo et al.⁴² founded application hybridized nano based materials in environmental protection. Yun et al.⁴³ determined degradation performance of nano-TiO₂ as a coating material used in roads and bridge construction. Sheikholeslami & Farshad⁴⁴ discussed the solar collector system with turbulater effect for hybrid nanoparticles. Hybrid nanofluid is useful to increase the exergy efficiency of solar system and produces higher overall efficiency⁴⁵.

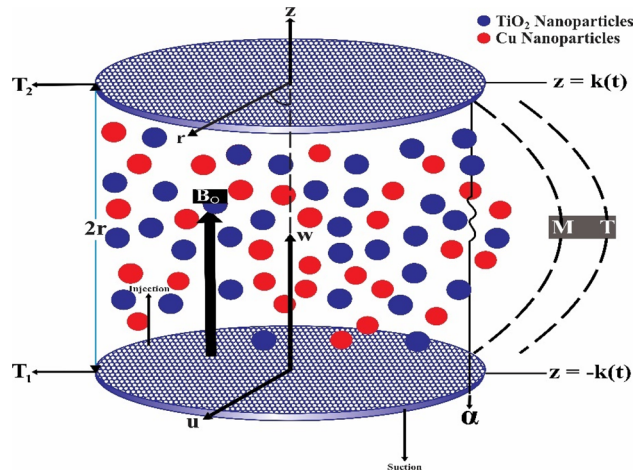


Figure 1. Physical model.

To the best of the author’s knowledge there has been a scarcity in research regarding analysis of morphology effect of hybrid nanofluids coupled with matrix metal and ceramic matrix nanocomposites on thermo physical features of fluid flow between two orthogonally placed porous disks. Mathematical modeling in the form of partial differential equations is developed by considering shape and size of different (MMNC) and (CMNC). Later on, attained PDE’s are converted into ODE’s by using appropriate variables. Solution of intricate coupled differential system is attained by implementing Runge–Kutta and shooting method jointly. Impact of involved dimensionless parameters on associated profiles is adorned.

Mathematical formulation

Let us consider an incompressible, viscous, laminar, unsteady, 2D flow of hybrid nanofluid containing TiO₂-Cu/water nanoparticles between two orthogonally moving porous coaxial disk in the presence of the external magnetic field applied in z-direction. The diameter of boundary disks is 2r. The physical model takes in a cylindrical coordinate system (r, θ, z) but velocity v disappears and u and w part of the velocity in the lines of r and z, respectively. The temperature at the lower disk is denoted by T₁ and the upper disk is T₂ show in Fig. 1.

Law of conservation of mass, momentum, and energy are as follows referred to Kashif et al.⁴⁶

$$\frac{\partial u}{\partial r} + \frac{u}{r} + \frac{\partial w}{\partial z} = 0 \tag{1}$$

$$\frac{\partial u}{\partial t} + u \frac{\partial u}{\partial r} + w \frac{\partial u}{\partial z} = -\frac{1}{\rho_{hnf}} \frac{\partial p}{\partial r} + \nu_{hnf} \left(\frac{\partial^2 u}{\partial r^2} + \frac{1}{r} \frac{\partial u}{\partial r} - \frac{u}{r^2} + \frac{\partial^2 u}{\partial z^2} \right) - \frac{\sigma_e B_0^2}{\rho_{hnf}} u \tag{2}$$

$$\frac{\partial w}{\partial t} + u \frac{\partial w}{\partial r} + w \frac{\partial w}{\partial z} = -\frac{1}{\rho_{hnf}} \frac{\partial p}{\partial z} + \nu_{hnf} \left(\frac{\partial^2 w}{\partial r^2} + \frac{1}{r} \frac{\partial w}{\partial r} + \frac{\partial^2 w}{\partial z^2} \right) \tag{3}$$

$$\frac{\partial T}{\partial t} + u \frac{\partial T}{\partial r} + w \frac{\partial T}{\partial z} = \alpha_{hnf} \frac{\partial^2 T}{\partial z^2} \tag{4}$$

where ρ_{hnf} is the density of (HN_{fd}), σ_e is the electrical conductivity, B_0^2 of themagnetic field is the strength, p is the pressure and T is the temperature, α_{hnf} is the thermal diffusivity, ν_{hnf} is the kinematics viscosity of the (HN_{fd}).

Thermophysical Properties of hybrid nanofluid referred to^{47–49}. Thermophysical properties of (N_{fd}) convective hybrid (TiO₂ – Cu/H₂O) then $\varphi_1 = \varphi_{TiO_2}$, $\varphi_2 = \varphi_{Cu}$, $\rho_{s1} = \rho_{TiO_2}$, $\rho_{s2} = \rho_{Cu}$, $(\rho c_p)_{s1} = (\rho c_p)_{TiO_2}$, $(\rho c_p)_{s2} = (\rho c_p)_{Cu}$, $k_{s1} = k_{TiO_2}$ and $k_{s2} = k_{Cu}$.

Effective dynamic viscosity. Efsa et al.⁴⁸ delivered a theory of diameter depending viscosity

$$\mu_{hnf} = \mu_{bf} (1 + 0.1008((\varphi_1)^{0.69574} (dp_1)^{0.44708} + (\varphi_2)^{0.69574} (dp_2)^{0.44708})) \tag{5}$$

Effective density. The effective density of HN_{fd} is denoted by the ρ_{hnf}

$$\rho_{hnf} = \varphi_1 \rho_{s1} + \varphi_2 \rho_{s2} - (1 - \varphi_1 - \varphi_2) \rho_{bf} \tag{6}$$

where φ_1 and φ_2 shows volume fraction, ρ_{bf} represent the density of base fluid, ρ_{s1} or ρ_{s2} indicates the density of solid NP's, ρ_{hnf} the density of hybrid nanofluid.

Effective heat capacitance. Hybrid nanofluid effective heat capacitance is denoted by

$$\rho_{hnf} = \varphi_1(\rho_{cp})_{s1} + \varphi_2(\rho_{cp})_{s2} - (1 - \varphi_1 - \varphi_2)(\rho_{cp})_{bf} \tag{7}$$

where $(\rho_{cp})_{s1}$ and $(\rho_{cp})_{s2}$ specify the thermal capacitance for strong NP's and the thermal capacitance for (B_{fd}) is defined in $(\rho_{cp})_{bf}$.

Effective thermal conductivity. The thermal conductivity of hybrid nano fluid of specific size and shape factor of NP's is described as under

$$k_{hnf} = \frac{k_{s2} + (n_2 - 1)k_{mbf} - (n_2 - 1)\varphi_2(k_{mbf} - k_{s2})}{k_{s2} + (n_2 - 1)k_{mbf} + \varphi_2(k_{mbf} - k_{s2})} k_{mbf} \tag{8}$$

where

$$k_{mbf} = \frac{k_{s1} + (n_1 - 1)k_f - (n_1 - 1)\varphi_1(k_f - k_{s1})}{k_{s1} + (n_1 - 1)k_f + \varphi_1(k_f - k_{s1})} k_f$$

where k_{hnf} is thermal conductivity for (HN_{fd}) , k_{s1} and k_{s2} are thermal conductivity of solid nanoparticles, n_1 and n_2 are different size factors (spherical, bricks, plates, cylindrical), k_{bf} and k_{mbf} are thermal conductivity and shapes factor base fluid. Furthermore, different shape of first (Fe_3O_4), second (Al_2O_3), third (TiO_2) and fourth (Cu) NP's (n_1 and n_2) based on thermal conductivity of (HN_{fd}) . The thermal conductivity of copper nanoparticles is high than titanium oxide.

$$\nu_{hnf} = \frac{\mu_{hnf}}{\rho_{hnf}} \text{ and } \alpha_{hnf} = \frac{k_{hnf}}{(\rho c_p)_{hnf}}, \quad Pr = \frac{(\mu C_p)_{bf}}{k_{bf}} \tag{9}$$

where ρ_s and ρ_f are density for solid and fluid fractions, the specific capacitance for (HN_{fd}) $(\rho c_p)_{hnf}$, the (HN_{fd}) for the effect of thermal conductivity k_{hnf} .

For boundary situations the flow state is:

$$\begin{aligned} z = -k(t) \quad u = 0, w = -A_1 k'(t) \text{ at } T = T_1 \text{ and } z = k, u = 0 \\ w = A_1 k'(t) \text{ at } T = T_2 \end{aligned} \tag{10}$$

Here, A_1 is the metric of penetrability of the partition, and the dot represents the w.r.t time t derivative. Following similarity variables are used

$$\eta = \frac{z}{k} \quad u = -\frac{r\nu_f}{k^2} F_\eta(\eta, t) \quad w = \frac{2\nu_f}{k} F(\eta, t) \quad \theta = \frac{T - T_2}{T_1 - T_2} \tag{11}$$

and result

$$\frac{\nu_{hnf}}{\nu_f} F_{\eta\eta\eta\eta} + \alpha(3F_{\eta\eta} + \eta F_{\eta\eta\eta}) - 2FF_{\eta\eta\eta} - \frac{k^2}{\nu_f} F_{\eta\eta t} - \frac{\rho_f}{\rho_{hnf}} + MF_{\eta\eta} = 0 \tag{12}$$

$$\theta_{\eta\eta} + \frac{\nu_f}{\alpha_{hnf}} (\alpha\eta - 2F)\theta_\eta - \frac{k^2}{\alpha_{hnf}} \theta_t = 0 \tag{13}$$

Associated boundary conditions

$$\begin{aligned} \eta = -1, F = -R, F_\eta = 0, \theta = 1, \\ \text{and } \eta = 1, F = R, F_\eta = 0, \theta = 0, \end{aligned} \tag{14}$$

Here, $\alpha = \frac{kk'(t)}{\nu_f}$ is the wall expansion ratio, $R = \frac{A_1 kk'(t)}{2\nu_f}$ is the absorptivity Reynolds number, $Sc = \frac{\nu_f}{D}$ is the Schmidt number and $M = \frac{\sigma_e B_0^2 k^2}{\mu_f}$ is the magnetic parameter.

Finally, we set $F = f R$, and consider the case following Majdalani et al.⁵⁰ when α is a constant, $f = f(\eta)$ and $\theta = \theta(\eta)$, which leads to $\theta_t = 0$ and $f_{\eta\eta t} = 0$. Thus we have the following equations

$$\frac{\nu_{hnf}}{\nu_f} f_{\eta\eta\eta\eta} + \alpha(3f_{\eta\eta} + \eta f_{\eta\eta\eta}) - 2Rff_{\eta\eta\eta} - \frac{\rho_f}{\rho_{hnf}} Mf_{\eta\eta} = 0 \tag{15}$$

$$\theta_{\eta\eta} + \left((1 - (\varphi_1 + \varphi_2)) + (\varphi_1) \left(\frac{\rho_{cps1}}{\rho_{cpbf}} \right) + (\varphi_2) \left(\frac{\rho_{cps2}}{\rho_{cpbf}} \right) \right) \frac{k_{mbf}}{k_{hnf}} \frac{k_{bf}}{k_{mbf}} Pr(\alpha\eta - 2Rf)\theta_\eta = 0 \tag{16}$$

Boundary conditions at lower and upper wall of channel

$$\eta = -1; f = -1, f_\eta = 0, \theta = 1 \text{ and } \eta = 1; f = 1, f_\eta = 0, \theta = 0 \quad (17)$$

Quantities of engineering interest. Skin friction and Nusselt number at both porous walls are computed coefficients which are of engineering interest are computed in this section.

Skin friction coefficients. The C_{f1} and C_{f-1} are the representation of skin friction coefficient of lower and upper disk which is expressed as

$$C_{f-1} = \frac{\xi_{zr}|_{\eta=-1}}{\rho_f (k'A_1)^2} = \frac{(1 + 0.1008((\varphi_1)^{0.69574} (dp_1)^{0.44708} + (\varphi_2)^{0.69574} (dp_2)^{0.44708}))}{R_r} f''(-1), \quad (18)$$

$$C_{f1} = \frac{\xi_{zr}|_{\eta=1}}{\rho_f (k'A_1)^2} = \frac{(1 + 0.1008((\varphi_1)^{0.69574} (dp_1)^{0.44708} + (\varphi_2)^{0.69574} (dp_2)^{0.44708}))}{R_r} f''(1).$$

where $R_r = 4 \left(\frac{k}{r} \right) \left(\frac{1}{R} \right)^2$ stand for local Reynolds number and ξ_{zr} are shear stresses at the lower and upper disk in the radial direction, respectively,

$$\xi_{zr} = \mu_{hmf} \left(\frac{\partial u}{\partial z} \right) |_{\eta=-1} = \mu_{bf} (1 + 0.1008((\varphi_1)^{0.69574} (dp_1)^{0.44708} + (\varphi_2)^{0.69574} (dp_2)^{0.44708})) \left(\frac{r v_f}{k^3} \right) f''(-1)$$

$$\xi_{zr} = \mu_{hmf} \left(\frac{\partial u}{\partial z} \right) |_{\eta=1} = \mu_{bf} (1 + 0.1008((\varphi_1)^{0.69574} (dp_1)^{0.44708} + (\varphi_2)^{0.69574} (dp_2)^{0.44708})) \left(\frac{r v_f}{k^3} \right) f''(1)$$

Nusselt number. The calculation at the lower and upper disk for heat transfer rate (Nusselt numbers) $Nu|_{\eta=-1}$ and $Nu|_{\eta=1}$ are given as

$$Nu|_{\eta=-1} = \frac{ks_z}{\kappa_f (T_1 - T_2)} |_{\eta=-1} = -\frac{k_{hmf}}{k_f} \theta'(-1)$$

$$Nu|_{\eta=1} = \frac{ks_z}{\kappa_f (T_1 - T_2)} |_{\eta=1} = -\frac{k_{hmf}}{k_f} \theta'(1) \quad (19)$$

where here heat flux is denoted as s_z which is follows as,

$$s_z|_{\eta=-1} = -k_{hmf} \left(\frac{\partial T}{\partial z} \right) |_{\eta=-1} = -\frac{(T_1 - T_2)}{k} k_{hmf} \theta'(-1)$$

$$s_z|_{\eta=1} = -k_{hmf} \left(\frac{\partial T}{\partial z} \right) |_{\eta=1} = -\frac{(T_1 - T_2)}{k} k_{hmf} \theta'(1)$$

where $R = \frac{A_1 k k'(t)}{2\nu_f}$.

Numerical procedure. Since attained couple system of ODEs manipulated in Eqs. (28) and (29) are intricate in nature and it is boundary value conditions so solution is found numerically instead of analytical approaches. For numerical computations shooting method in conjunction with Runge–Kutta method is implemented. Due to low computation, stability and accurate results in less time, Runge–Kutta method is better choice. The main advantage of this method is speed (computational cost) and additivity of the method with the initial value problem. Because of the significant applications of initial value problems into the real world/practical applications that's why, to find the initial value problem with an appropriate shooting method is very successful.

Validation of the proposed method. In a shooting method, the missing initial condition at the initial point of the Interval is assumed, and the DE is then integrated numerically as an initial value problem. The accuracy of the assumed missing initial condition is then checked by comparing the calculated value of the dependent variable at the terminal point with its given value here. If a difference exist, another value of the missing initial condition must be assumed and the process is repeated. This process is continued until the agreement between the calculated and the given condition. For this purpose, given below Table 10 shows the convergence of our numerical results as the decrease in step-size gives us confidence on our computational procedure. Clearly, our boundary conditions satisfied with symmetric and accurate results of shear stress at lower wall as well.

An extensive representation of non-linear coupled system of ordinary differential equations along with coefficients possessing features of matrix composite materials and hybrid nano fluid

$$\left(\frac{(1 + 0.1008((\varphi_1)^{0.69574} (dp_1)^{0.44708} + (\varphi_2)^{0.69574} (dp_2)^{0.44708}))}{((1 - (\varphi_1 + \varphi_2)) + (\varphi_1) \left(\frac{\rho_{s1}}{\rho_{bf}}\right) + (\varphi_2) \left(\frac{\rho_{s2}}{\rho_{bf}}\right))} \right) f''''[\eta] - \alpha(3f''[\eta] + \eta f''''[\eta]) - 2Rf[\eta]f''''[\eta] - \left(\frac{1}{((1 - \varphi_1 - \varphi_2) + \varphi_1 \left(\frac{\rho_{s1}}{\rho_{bf}}\right) + \varphi_2 \left(\frac{\rho_{s2}}{\rho_{bf}}\right))} \right) Mf''[\eta] = 0 \tag{20}$$

$$\theta''[\eta] + \left((1 - (\varphi_1 + \varphi_2)) + (\varphi_1) \left(\frac{\rho_{cps1}}{\rho_{cpbf}}\right) + (\varphi_2) \left(\frac{\rho_{cps2}}{\rho_{cpbf}}\right) \right) \left(\frac{k_{s2} + (N - 1)k_{mbf} + \varphi_2(k_{mbf} - k_{s2})}{k_{s2} + (N - 1)k_{mbf} - (N - 1)\varphi_2(k_{mbf} - k_{s2})} \right) \left(\frac{k_{s1} + (N - 1)k_{bf} + \varphi_1(k_{bf} - k_{s1})}{k_{s1} + (N - 1)k_{bf} - (N - 1)\varphi_1(k_{bf} - k_{s1})} \right) Pr(\alpha\eta - 2Rf[\eta])\theta'[\eta] = 0 \tag{21}$$

$$H_1 = \left(\frac{(1 + 0.1008((\varphi_1)^{0.69574} (dp_1)^{0.44708} + (\varphi_2)^{0.69574} (dp_2)^{0.44708}))}{((1 - (\varphi_1 + \varphi_2)) + (\varphi_1) \left(\frac{\rho_{s1}}{\rho_{bf}}\right) + (\varphi_2) \left(\frac{\rho_{s2}}{\rho_{bf}}\right))} \right) \tag{22}$$

$$H_2 = \left(\frac{1}{((1 - \varphi_1 - \varphi_2) + \varphi_1 \left(\frac{\rho_{s1}}{\rho_{bf}}\right) + \varphi_2 \left(\frac{\rho_{s2}}{\rho_{bf}}\right))} \right) \tag{23}$$

$$H_3 = \left((1 - (\varphi_1 + \varphi_2)) + (\varphi_1) \left(\frac{\rho_{cps1}}{\rho_{cpbf}}\right) + (\varphi_2) \left(\frac{\rho_{cps2}}{\rho_{cpbf}}\right) \right) \tag{24}$$

$$D_1 = \left(\frac{k_{s2} + (N - 1)k_{mbf} + \varphi_2(k_{mbf} - k_{s2})}{k_{s2} + (N - 1)k_{mbf} - (N - 1)\varphi_2(k_{mbf} - k_{s2})} \right) \tag{25}$$

$$D_2 = \left(\frac{k_{s1} + (N - 1)k_{bf} + \varphi_1(k_{bf} - k_{s1})}{k_{s1} + (N - 1)k_{bf} - (N - 1)\varphi_1(k_{bf} - k_{s1})} \right) \tag{26}$$

$$\omega = D_1 D_2 \tag{27}$$

Putting values of (Eq. 22), (Eq. 23), (Eq. 24), (Eq. 25), (Eq. 26) and (Eq. 27) in Eqs. (Eq. 20) and (Eq. 21) or final result are

$$H_1 f''''[\eta] - \alpha(3f''[\eta] + \eta f''''[\eta]) - 2Rf[\eta]f''''[\eta] - H_2 Mf''[\eta] = 0 \tag{28}$$

$$\theta''[\eta] + H_3 \omega Pr(\alpha\eta - 2Rf[\eta])\theta'[\eta] = 0 \tag{29}$$

Solution of the problem. We followed the RK methodology with the inclusion of shooting methods for the solution purpose of the existing flow model. The following replacement remain ingredient to start the process:

$$q_1^* = f[\eta], \quad q_2^* = f'[\eta], \quad q_3^* = f''[\eta], \quad q_4^* = f'''[\eta], \quad q_5^* = \theta[\eta], \quad q_6^* = \theta'[\eta]$$

First, transform the model system of ODEs (Eq. 28) and (Eq. 29) in the following pattern,

$$f''''[\eta] = \frac{1}{H_1} (f''''[\eta](-\alpha\eta + Rf[\eta]) + f''[\eta](3\alpha + 2Rf'[\eta]) + H_2 Mf_{\eta\eta})$$

$$\theta''[\eta] = -H_3 \omega Pr(-\alpha\eta + 2Rf[\eta])\theta'[\eta]$$

By interchanging, embedded in Eq. (25), the following system is attained:

$$\begin{bmatrix} q_1^* \\ q_2^* \\ q_3^* \\ q_4^* \\ q_5^* \\ q_6^* \end{bmatrix}' = \begin{bmatrix} q_2^* \\ q_3^* \\ q_4^* \\ \frac{1}{H_1} (f''''[\eta](-\alpha\eta + Rf[\eta]) + f''[\eta](3\alpha + 2Rf'[\eta]) + H_2 Mf_{\eta\eta}) \\ q_5^* \\ -H_3 \omega Pr(-\alpha\eta + 2Rf[\eta])\theta'[\eta] \end{bmatrix}$$

Consequently, the initial condition are:

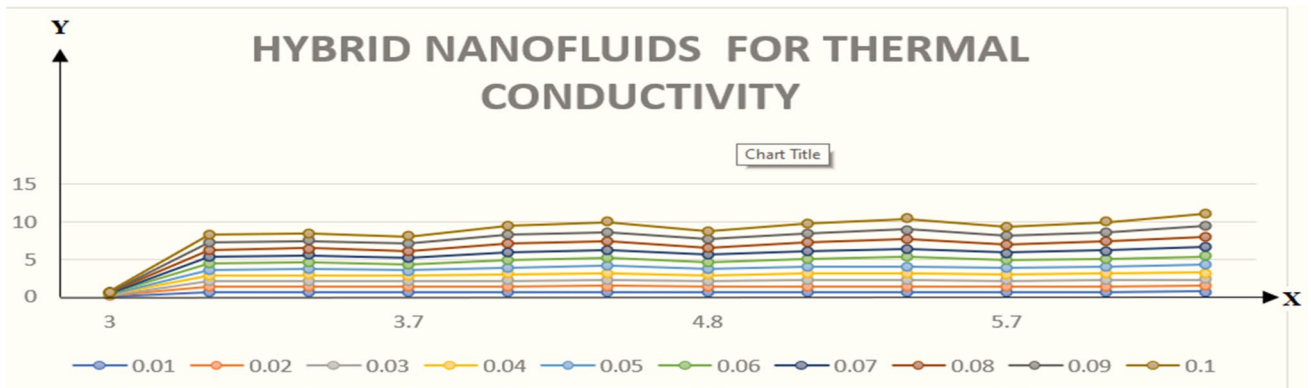


Figure 2. Suggested thermal conductivity behavior for HN_{fd} .

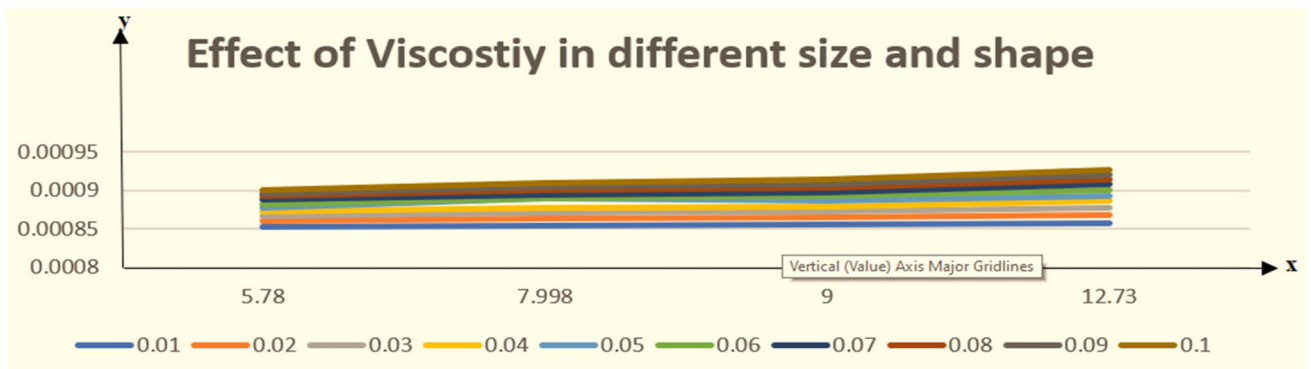


Figure 3. Influence of the scale of hybrid NPs under the viscosity.

$$\begin{bmatrix} q_{1(\eta=-1)}^* \\ q_{2(\eta=-1)}^* \\ q_{3(\eta=1)}^* \\ q_{4(\eta=1)}^* \\ q_{5(\eta=-1)}^* \\ q_{6(\eta=1)}^* \end{bmatrix} = \begin{bmatrix} -1 \\ 0 \\ a \\ b \\ 1 \\ 0 \end{bmatrix}$$

where a and b missing initial conditions, now, above system with suitable initial condition (gauss values) is solved until achieved the required accuracy with help of Mathematica.

Result and discussion:

This section is presented to elaborate the impact of flow concerning equations like expansion/contraction ratio parameter α , permeable Reynold parameter, magnetic parameter, volume friction parameter on velocity and temperature profile are elaborated through Figs. 2, 3, 4, 5, 6, 7, 8, 9, 10, 11, 12. In addition quantities of engineering interest like shear stress coefficients at lower and upper walls along with heat fluxes are computed numerically against involved variables. Assurance of presently computed data is done by constructing comparison with previously published literature. Thermophysical features like specific heat, density and thermal conductivity of nanoparticles and base fluid is numerically presented in Table 1. Table 2 expresses variation in the effect of shape and size factor of hybrid nanoparticles on heat transfer coefficient by fixing $\varphi_1 = \varphi_2 = 0.01, Sc = 1, M = 1, R = -1, Pr = 6.2, \alpha = -1$. It is seen from attained values that by increasing magnitudes of n_1 and n_2 the coefficient of convective heat transfer increases. Tables 3 and 4 demonstrates the influence of the φ_2, R, α on skin friction and the Nusselt amount for (Cu–water) and hybridized (TiO₂ – Cu/water) nanofluid for various shapes (sphere, stone, cylindrical, plates) of nanoparticles. It is established that nanofluid and hybrid nano fluid has correlation with skin friction and heat flux coefficients. It is also evident that the amount of Nusselt rises with φ_2 and R and decreases against α . It is also depicted that skin friction coefficient for hybrid nanofluid is lower than the skin friction coefficient for nanofluid and the skin friction coefficient for hybrid nanofluid is higher than the skin friction coefficient for nanofluid which indicates that hybridized nano fluid is much better that ordinary nanofluid. The effect of Prandtl number and volume fraction φ_1 and φ_2 on Nusselt number and skin friction coefficient are shown in Table 5. Table 5 also shows that by increasing volume fractions φ_1 and φ_2 and by fixing Prandtl number the skin friction and Nusselt number increases. The reason behind this fact is that Prandtl number is the ratio of diffusive momentum to thermal diffusivity so by increasing

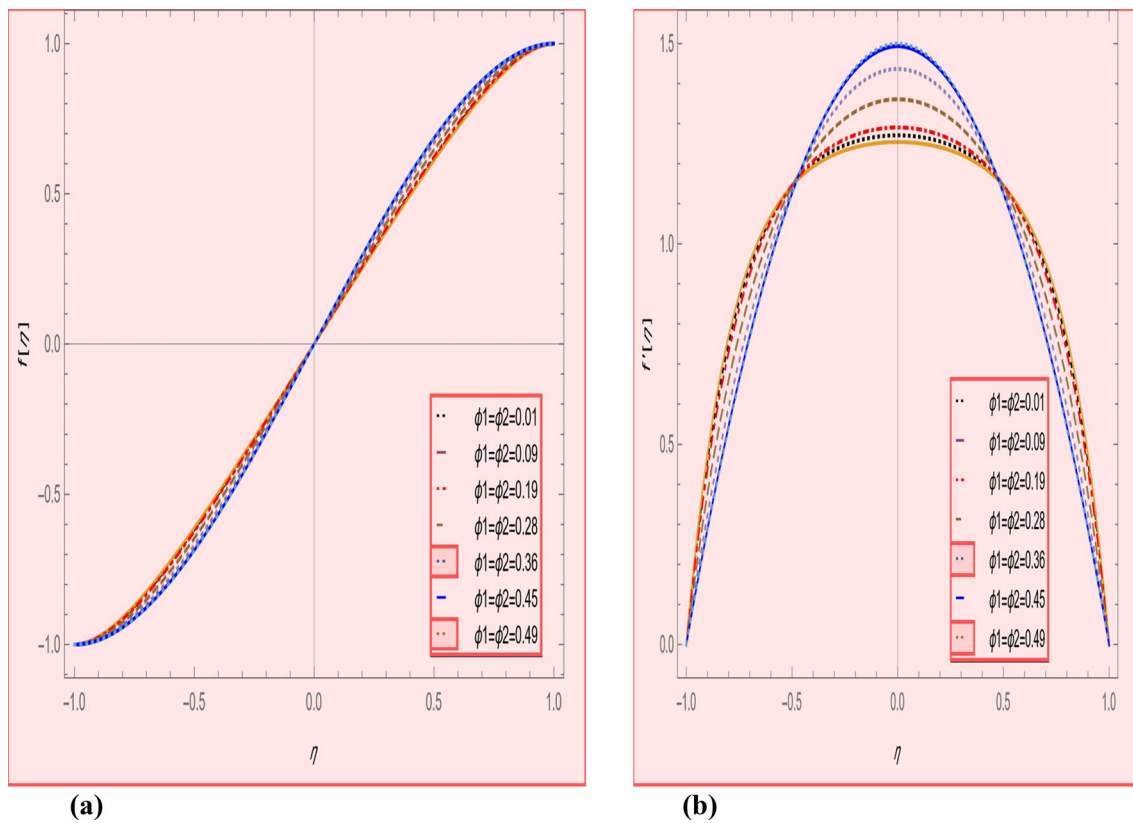


Figure 4. (a) Axial, (b) radial velocity profile effect in volume fraction for $\alpha = -4, R = -1, M = 1, SC = 1, Pr = 6.2$.

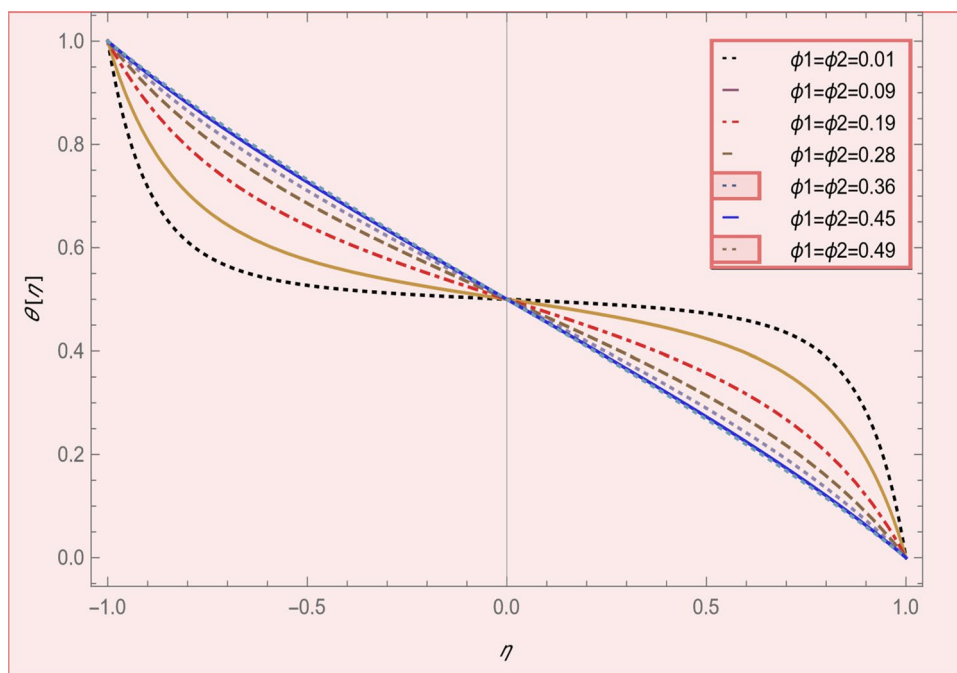


Figure 5. Temperature profile effect in volume fraction for $\alpha = -4, R = -1, M = 1, SC = 1, Pr = 6.2$.

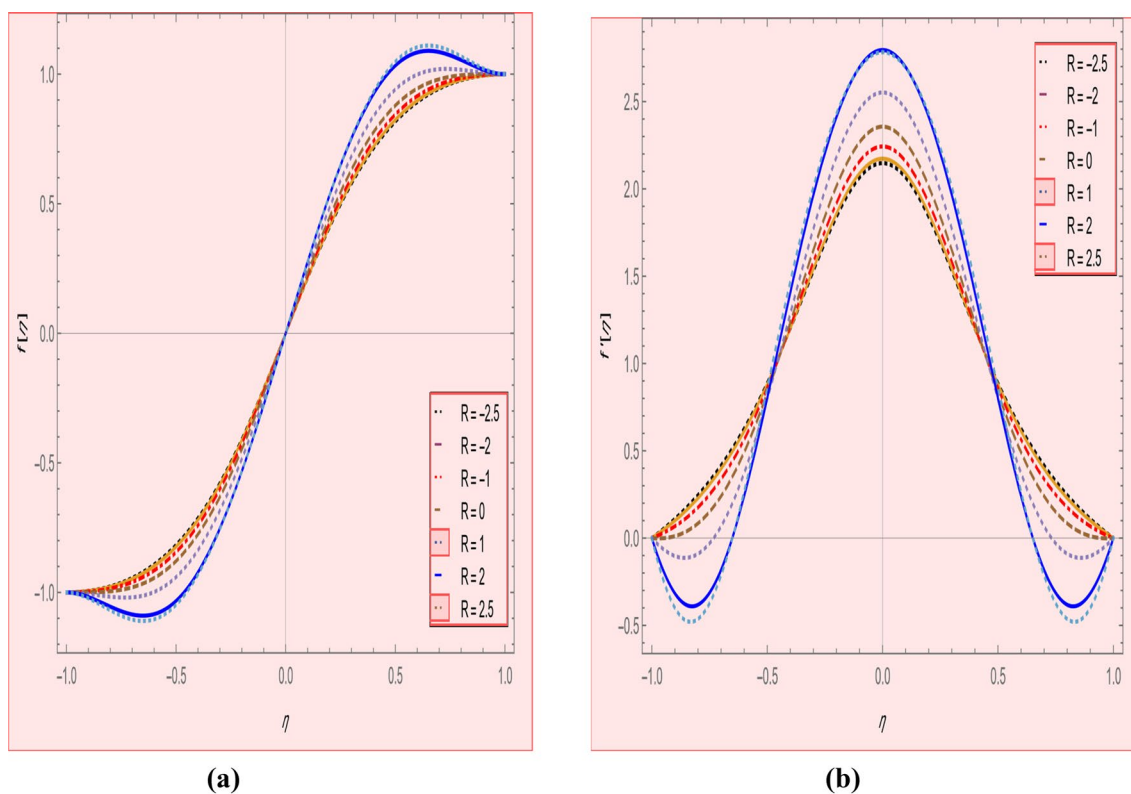


Figure 6. (a) Axial, (b) radial velocity profile effect in Reynolds number for $\alpha = 5, \varphi_1 = \varphi_2 = 0.01, M = 1, SC = 1, Pr = 6.2$.

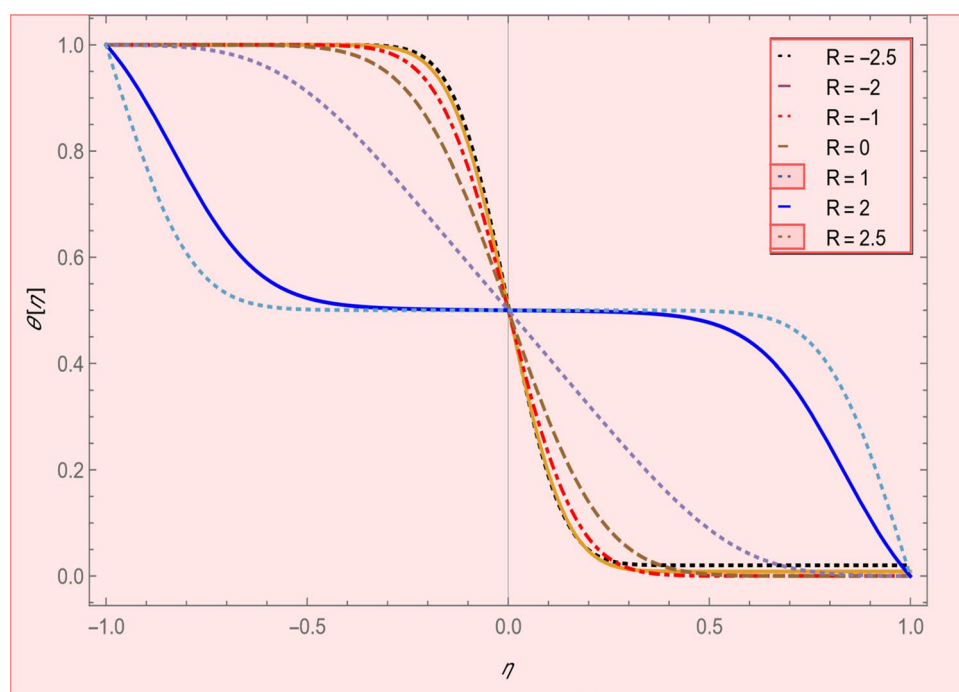


Figure 7. Temperature profile effect permeable Reynolds number for $\alpha = 5, \varphi_1 = \varphi_2 = 0.01, M = 1, SC = 1, Pr = 6.2$.

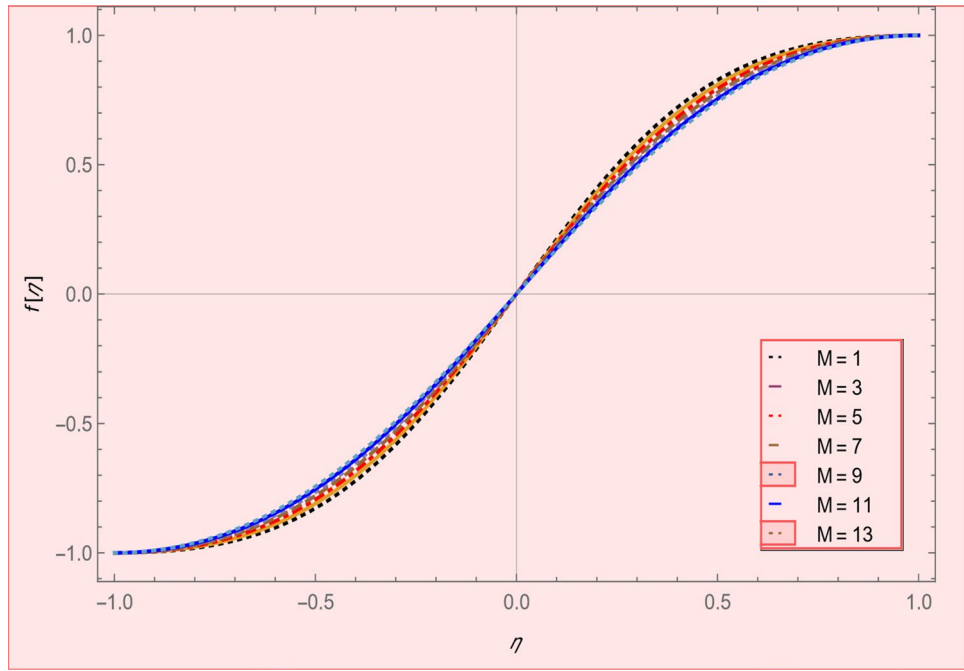


Figure 8. Axial velocity profile effect in magnetic parameter for $\alpha = 4, R = -1, \varphi_1 = \varphi_2 = 0.04, SC = 1, Pr = 6.2$.

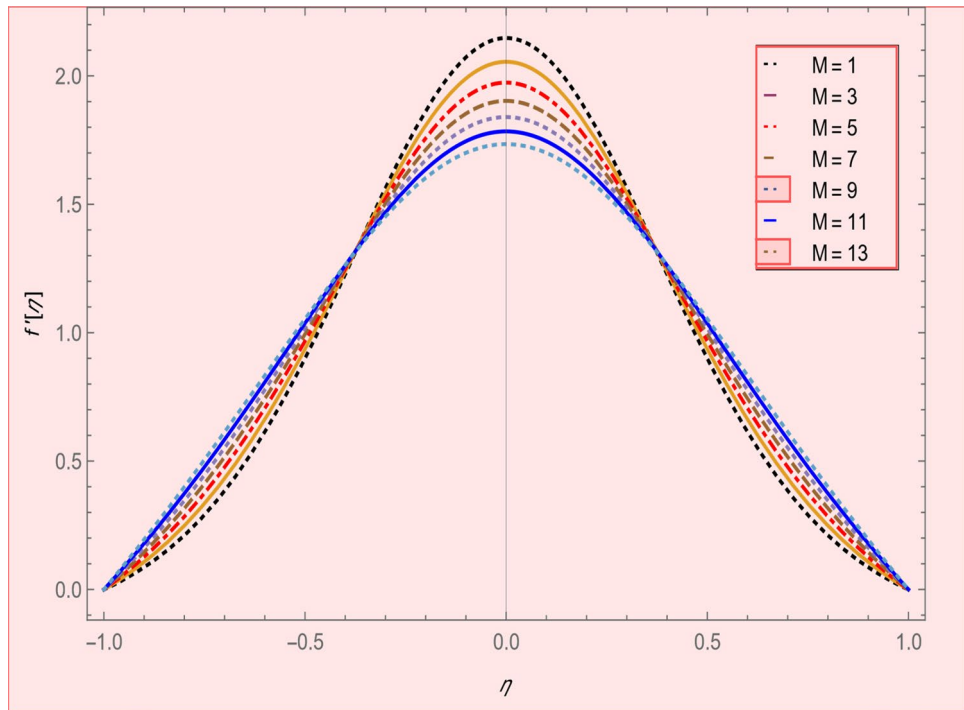


Figure 9. Radial velocity effect in magnetic parameter profile for $\alpha = 4, R = -1, \varphi_1 = \varphi_2 = 0.04, SC = 1, Pr = 6.2$.

(Pr) momentum diffusivity enhances which as an outcome raises heat flux coefficient. Table 6 shows impact of magnetic parameter and permeable Reynold number on skin friction and heat transfer in Table 6. It is observed that for $R < 0$ or $R > 0$ and $\alpha < 0$ or $\alpha > 0$ the skin friction coefficient and Nusselt number increases against (M). Table 7 displays the effect of injection/suction parameter α skin friction coefficient and Nusselt number rises. It is also evidenced that $R = 1$ and $R = -1$ and by assuming (α) less or greater than zero skin friction coefficient

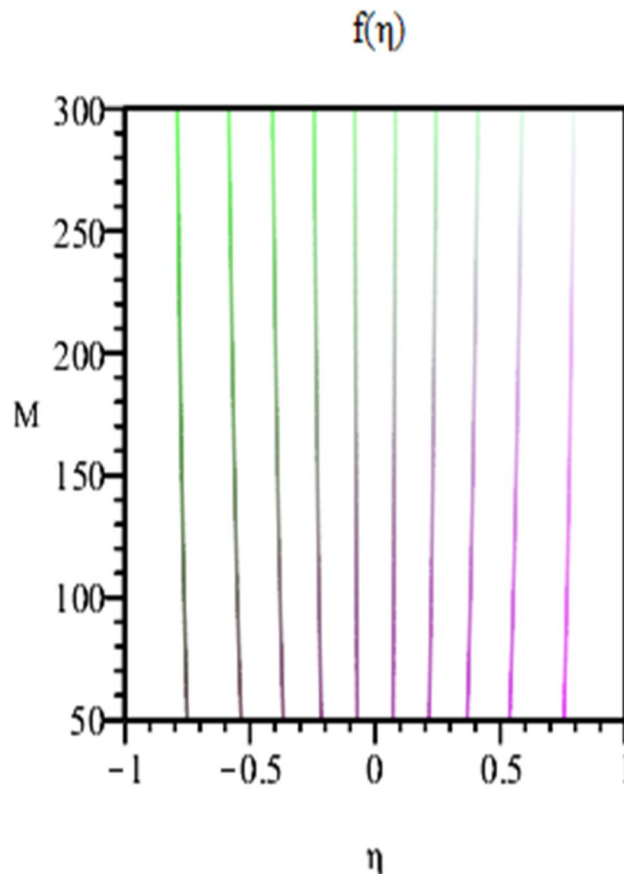


Figure 10. Contour of Axial velocity for $\varphi_1 = \varphi_2 = 0.01$, $Sc = 1$, $\alpha = 3$, $Re = -1$, $Pr = 6.2$.

and heat transfer of Nusselt number decrease for both porous disks. Table 8 shows impact of different physical parameters which effect skin friction and Nusselt number coefficients. It is found that by decreasing magnetic parameter skin friction coefficient decreases and the Nusselt number and associated thermal boundary layer thickness increases. Specifically it is noticed that by increasing (Pr) skin friction coefficient decreases and Nusselt number increases. The reason behind this fact is that by increasing Prandtl number momentum diffusivity enhances which as an outcome increases average kinetic energy of molecules and heat flux increases and resistance provided by surface to fluid decreases. Table 9 shows credibility of work by constructing comparison with previously published literature presented by Kashif et al.⁴⁶. Table 10 shows numerical stability of results for $f(-1)$, $f'(-1)$ and $f''(-1)$ at different values of η .

Figure 2 expresses variation in thermal conductivity against φ_1 and φ_2 and by considering four different shapes (spherical, plates, bricks, cylindrical) of hybrid nanoparticles. We observed that higher thermal conductivity performance is achieved at 5.7 when particles volume fractions is at magnitude 0.1. It means if we gradually increase the numerical values of φ_1 and φ_2 and shape factor along with volume fractions thermal conductivity increases. In Fig. 3 it is observed that the viscosity base fluid (water) depends on volume fraction φ , diameter (dp_1 and dp_2) of particles. It is manifested that as we increase volume fraction of nanoparticles it causes internal shear stress to enhance which will, in turn, increases the viscosity of (HNFDs). The increase in hydrodynamic diameter of nano structures as a result adsorption and clustering will lead to enhance the viscosity. Furthermore, the effect of viscosity is very high for size factor 12.73 when particles volume fraction φ_1 and φ_2 is 0.1 We observed that in Figs. 2 and 3 if we are increasing the values of volume fraction and shape or size factor increases thermal conductivity and viscosity will arise. Figures 4 and 5 represents the impact of volume fraction parameter on axial, radial velocity components and on temperature profile for fixed values for $\alpha = -4$, $R = -1$, $M = 1$, $Sc = 1$, $Pr = 6.2$. It is observed that volume fraction parameter causes decrease in axial and radial component of velocity. Physically, it is due to the reason that heat is dissipated with deformation in shape of nanoparticles. In addition uplift in nanoparticle volume fraction will consumes more energy and thermal boundary layer thickness raises. Figures 6, 7 shows effect of permeable Reynold number on the axial and radial velocity and temperature profile. Physically, it is worth noting that the amount of Reynold produces inertial effect and as an outcome viscosity reduces and velocity increases. Figures 8, 9 displays impact of magnetic parameter on axial and radial velocity profile. It is observed that by increasing (M) axial component of velocity increases whereas radial velocity component decreases. This is because of the fact that by increasing (M) Lorentz forces are generated which reduces momentum of fluid particles in axial direction. From this statement, we can conclude that the velocity of fluid is normalized by the transverse application magnetic field. The vibration of the particles within the fluid which

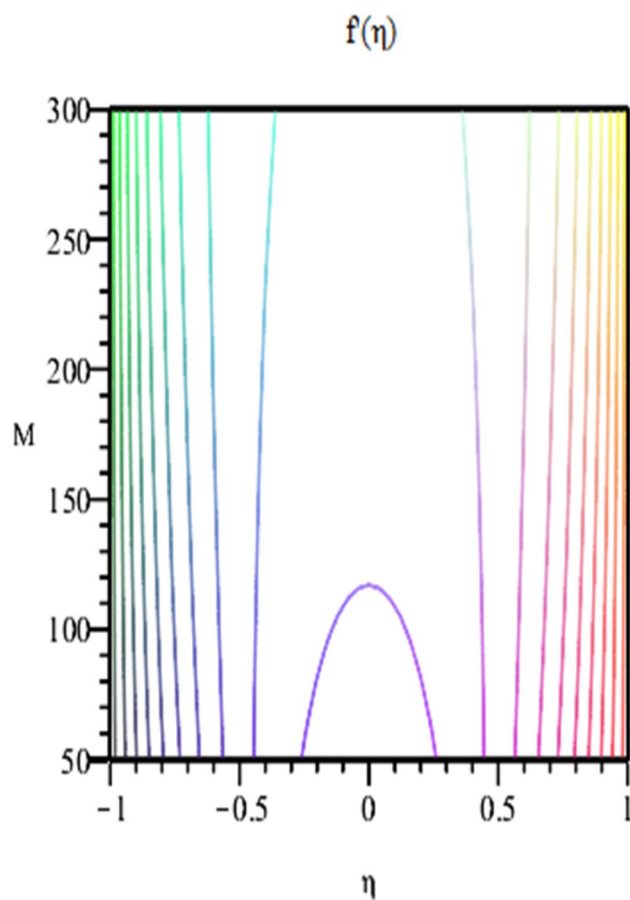


Figure 11. Contour of Radial velocity for $\varphi_1 = \varphi_2 = 0.01, Sc = 1, \alpha = 3, Re = -1, Pr = 6.2$.

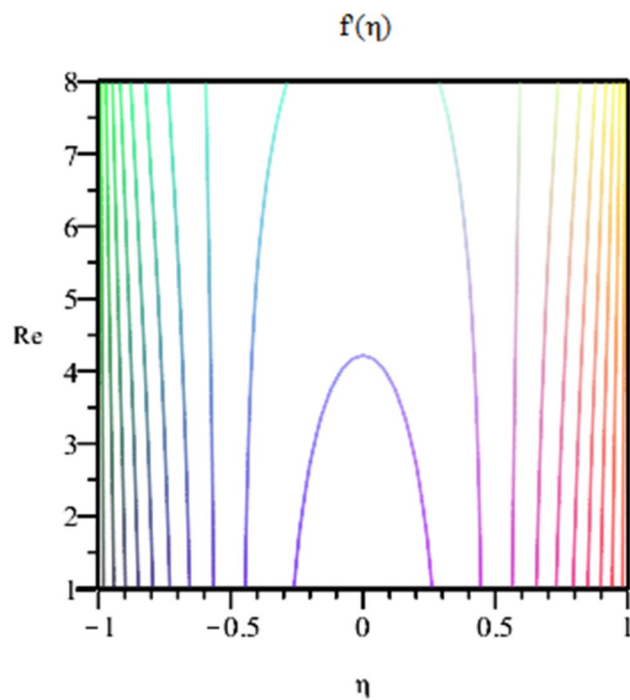


Figure 12. Contour of Radial velocity with increasing of Reynolds number fields for $\varphi_1 = \varphi_2 = 0.01, Sc = 1, \alpha = 3, M = 50, Pr = 6.2$.

Physical properties	H ₂ O (f)	Fe ₃ O ₄	Al ₂ O ₃	TiO ₂	Cu
ρ (kg m ⁻³)	997.0	5180	3970	4250	8933
(J k g ⁻¹ k ⁻¹)	4180	670	765	686.2	385
κ (wm ⁻¹ k ⁻¹)	0.6071	9.7	40	8.9538	400

Table 1. Thermophysical features of HN_{fd} and NP's.

Types	$n_1 = 3$				$n_2 = 3$			
	$n_2 = 3$	$n_2 = 3.7$	$n_2 = 4.8$	$n_2 = 5.7$	$n_1 = 3$	$n_1 = 3.7$	$n_1 = 4.8$	$n_1 = 5.7$
HNF1	0.01755	0.01798	0.01866	0.01922	0.01755	0.01785	0.01829	0.01862
HNF2	0.01763	0.01791	0.01832	0.01863	0.01763	0.01808	0.01881	0.01941
HNF3	0.01789	0.01835	0.01909	0.01969	0.01789	0.01831	0.01897	0.01949
HNF4	0.01814	0.0186	0.01933	0.01994	0.01814	0.0186	0.01934	0.01994

Table 2. Effect of shape and size factor of HN_{fd} on heat transfer coefficient by fixing $\varphi_1 = \varphi_2 = 0.01, Sc = 1, M = 1, R = -1, Pr = 6.2, \alpha = -1$.

Cu-water							
φ_2	R	α	$ C_f _{\eta=-1}$	$ Nu_z(3) _{\eta=-1}$	$ Nu_z(3.7) _{\eta=-1}$	$ Nu_z(4.8) _{\eta=-1}$	$ Nu_z(5.7) _{\eta=-1}$
0.02	0.1	1	2.4499	0.09544	0.09690	0.09894	0.10042
0.03			2.4416	0.10011	0.10229	0.10533	0.10753
0.04			2.4341	0.10482	0.10772	0.11175	0.11465
0.05			2.4275	0.10958	0.11318	0.11818	0.12177
0.05	0	1	2.3933	0.063041	0.06592	0.06998	0.7294
	0.1		2.4275	0.10958	0.11318	0.11818	0.12176
	0.2		2.4643	0.18506	0.18893	0.19424	0.19800
	0.3		2.5036	0.30192	0.30502	0.30921	0.31215
0.05	0.1	0.3	2.9831	0.44841	0.44938	0.45068	0.45158
		0.5	2.8218	0.30755	0.31061	0.31476	0.31766
		0.7	2.6626	0.20636	0.21021	0.21545	0.21916
		1	2.4275	0.10958	0.11318	0.11818	0.12177

Table 3. Numerical variation in shear stress at the lower porous wall with different shape factors for $\varphi_2, \varphi_1 = 0, R, \alpha$ (Cu-water) (N_{fd}).

TiO ₂ - Cu/water							
φ	R	α	$ C_f _{\eta=-1}$	$ Nu_z(3) _{\eta=-1}$	$ Nu_z(3.7) _{\eta=-1}$	$ Nu_z(4.8) _{\eta=-1}$	$ Nu_z(5.7) _{\eta=-1}$
0.02	0.1	1	2.3728	0.10655	0.11044	0.11629	0.12087
0.03			2.3345	0.11709	0.12298	0.13178	0.13862
0.04			2.3023	0.12782	0.13569	0.14737	0.15635
0.05			2.2761	0.13869	0.14849	0.16290	0.17385
0.05	0	1	2.2412	0.08707	0.09569	0.10876	0.11899
	0.1		2.2761	0.13869	0.14849	0.16290	0.17385
	0.2		2.3141	0.21577	0.22543	0.23926	0.24950
	0.3		2.3557	0.32667	0.32667	0.34377	0.35099
0.05	0.1	0.3	2.9276	0.45573	0.45784	0.46074	0.46281
		0.5	2.7380	0.33074	0.33780	0.34765	0.35478
		0.7	2.5510	0.23612	0.24554	0.25893	0.26880
		1	2.2760	0.13869	0.14849	0.16290	0.17386

Table 4. Numerical variation in shear stress against $\varphi = \varphi_1 = \varphi_2, R, \alpha$ (TiO₂ - Cu/water) (HN_{fd}).

$\varphi_1 = \varphi_2$	Pr	$ C_f _{\eta=-1}$	$ Nu_z _{\eta=-1}$
0.01 = 1%	5.5	3.3953	0.0269
0.02 = 2%	5.5	3.3959	0.0324
0.03 = 3%	5.5	3.3964	0.0385
0.04 = 4%	5.5	3.3969	0.0452
0.01 = 1%	6.2	3.3953	0.0147
0.01 = 1%	6.7	3.3953	0.0131
0.01 = 1%	6.9	3.3953	0.0115

Table 5. Variation in C_f and Nu_z against (Pr) and volume fraction φ_1, φ_2 for (Cu-TiO₂/water) hybrid nanofluid when $\alpha = -1, R = -1, M = 1$.

M	R	$\alpha = -1$		$\alpha = 1$	
		$ C_f _{\eta=-1}$	$ Nu_z _{\eta=-1}$	$ C_f _{\eta=-1}$	$ Nu_z _{\eta=-1}$
1	-1.5	3.1641	0.000611	2.0856	0.0000014
3	-1	3.6742	0.018523	2.4389	0.0000594
6	-0.5	4.3941	0.35553	3.0194	0.0021022
9	0	5.1767	2.31074	3.6834	0.0526765
11	0.5	5.8919	5.40947	4.284	0.6776833
13	1	6.6616	8.46962	5.4229	5.8166543
15	1.5	6.40676	6.61847	6.2224	8.744112

Table 6. Variation in C_f and Nu_z against (M) and (R) for (HN_{fd}) (Cu-TiO₂/water) when $\varphi_1 = \varphi_2 = 0.01, \alpha = -1, Sc = 1, Pr = 6.2$.

α	$Re = 1$		$Re = -1$	
	$ C_f _{\eta=-1}$	$ Nu_z _{\eta=-1}$	$ C_f _{\eta=-1}$	$ Nu_z _{\eta=-1}$
-3	7.1043	14.253	4.8889	1.65409
-2	6.0398	11.364	4.1151	0.23546
-1	4.9781	8.4941	3.3953	0.017631
0	3.9204	5.6703	2.7374	0.0010334
1	2.8672	3.0214	2.1478	0.000055
2	1.8173	1.039	1.6314	0.0000027
3	0.7643	0.20338	1.1904	1.320×10^{-7}

Table 7. Variation in C_f and Nu_z against α for (HN_{fd}) (Cu-TiO₂/water) when $\varphi_1 = \varphi_2 = 0.01, M = 1, Sc = 1, Pr = 6.2$.

is controlled by the Lorentz force is due to the magnetic effect. Figure 10 represents variation in velocity against (M) through contour lines. It is depicted that contour lines are roughly flat in the area of the midpoint of η and negligible reducing pattern along the problem's boundary. Figure 11 displays the contour of the influence of variable M on the radial velocity. In Fig. 11 contour lines representing variation in radial component of velocity is sketched which shows optimized change in velocity against η at boundaries whereas at center these lines shows zero change. Figure 12 indicates that the contours lines are very similar to the problem's boundaries as opposed to the center of an area and contributes to the radial velocity maximum being placed in the center of an area. The contour of radial velocity with the variance of parameter R was seen in Fig. 12. It is also noticed that contour lines expand against the boundaries of the main problem and expand in the major component of the field with an appreciation in the value of R which contributes to a reduction in the radial velocity with a fall in the amount of R .

α	R	M	φ_1	φ_2	n_1	n_2	Pr	$ C_f _{\eta=-1}$	$ Nu_z _{\eta=-1}$
0.1	0.01	1	0.01	0.01	3	3	6.2	3.1080	0.43022
0.2								3.0262	0.35087
0.3								2.9437	0.28423
0.4								2.8623	0.22881
	-0.02							3.0801	0.33628
	-0.03							3.0591	0.27383
	-0.04							3.0485	0.24645
		1						2.7231	0.43041
		2						2.5132	0.43053
		3						2.2893	0.43065
			0.02					3.0999	0.43221
			0.03					3.0922	0.43419
			0.04					3.0848	0.43607
				0.02				3.1031	0.43198
				0.03				3.0984	0.43367
				0.04				3.0939	0.43533
					3.7			3.1080	0.43022
					4.8			3.1080	0.43066
					5.7			3.1080	0.43118
						3.7		3.1080	0.43051
						4.8		3.1080	0.43089
						5.7		3.1080	0.43118
							4.5	3.1080	0.44852
							5.2	3.1080	0.44094
							5.5	3.1080	0.43767

Table 8. Variation in skin friction coefficient and Nusselt number at lower wall.

φ^{50}	$\varphi_1 + \varphi_2$	$\alpha > 0^{46}$	Present work	$\alpha < 0^{46}$	Present work
0%	0%	1.6794	1.6797	3.1664	3.1766
5%	5%	1.9174	1.9197	3.6112	3.6123
10%	10%	2.2135	2.2158	4.1606	4.1616
15%	15%	2.5839	2.5849	4.8430	4.8550
20%	20%	3.0519	3.0529	5.6988	5.6998

Table 9. Comparison of Nusselt number at lower porous wall with results published by Kashif et al.⁴⁶ against φ and α .

Conclusion

In this study numerical analysis of MHD hybrid nanofluids flows through porous surfaces is adumbrated. Thermophysical features of metallic and ceramic-metallic nanocomposites are combined with hybrid nanofluid. Evaluation about shape, size factors and particle volume fraction on velocity, temperature profile is executed. Numerical and graphical consequences are gained regarding skin friction coefficient and Nusselt number.

Some key findings are itemized as below

- (1) Nusselt number at $n = 5.7$ shows good results in MMNC than shape factors at both porous walls.
- (2) Magnetic parameters have a significant effect on skin friction and Nusselt number for hybrid flow.
- (3) In absence of injection/suction all governing parameters at lower porous surface show good performance as compared to upper surface.
- (4) Hybrid nanofluids under the effect of M and R indicate better results as compared to nanofluids.
- (5) For the contracting case Nusselt and skin friction coefficients for hybrid nanofluid show significant results.
- (6) Increase in volume fraction thermal boundary layer thickness increases but permeable Reynold number reduces thermal boundary layer thickness.

η	$f(-1)$	$f'(-1)$	$f''(-1)$
-1	-1	0	2.8682185248890812
-0.9	-0.986004632148899	0.2762900573162856	2.6513635499005477
-0.8	-0.9455224728264963	0.5291984277529419	2.4022339523123413
-0.7	-0.8810372014384086	0.7559667541088714	2.129942115638948
-0.6	-0.7952655915371383	0.9546625435491819	1.8418610445096326
-0.5	-0.6910837969233515	1.1240010434185939	1.5435889317798919
-0.4	-0.5714712122097215	1.263175625521357	1.2391316972955884
-0.3	-0.4394701755700228	1.371712201118385	0.93118511715582
-0.2	-0.29815875720869417	1.4493534762608988	0.6214396059796121
-0.1	-0.1506336107568336	1.4959731677879262	0.31087067312291067
0	$1.55484340680353 \times 10^{-10}$	1.5115177949361303	$1.2913497632327 \times 10^{-9}$
0.1	0.1506336107568336	1.4959731683236508	0.31087067312291067
0.2	0.29815875720869417	1.4493534762608988	0.6214396059796121
0.3	0.4394701755700228	1.371712201118385	0.93118511715582
0.4	0.5714712122097215	1.263175625521357	1.2391316972955884
.5	0.6910837969233515	1.1240010434185939	1.5435889317798919
0.6	0.7952655915371383	0.9546625435491819	1.8418610445096326
0.7	0.8810372014384086	0.7559667541088714	2.129942115638948
0.8	0.9455224728264963	0.5291984277529419	2.4022339523123413
0.9	0.986004632148899	0.5291984277529419	2.6513635499005477
1	1	0	2.8682185248890812

Table 10. Data for the Numerical Stability.

Received: 28 September 2020; Accepted: 23 April 2021

Published online: 10 June 2021

References

- Choi, S. U. S., & Eastman, J. A. Enhance thermal conductivity of fluids with nanoparticles, in *International Mechanical Engineering Congress and Exhibition, San Francisco, CA (United States)*, 12–17 Nov 1995.
- Yamada, A., Sasabe, H., Osada, Y. & Shiroda, I. *Concepts of Hybrid Materials, Concept and Case Studies* (ASM International, 1989).
- Chu, Y.-M., Ali, R., Asjad, M. I., Ahmadian, A. & Senu, N. Heat transfer flow of Maxwell hybrid nanofluids due to pressure gradient into rectangular region. *Sci. Rep.* **10**, 1643 (2020).
- Zeeshan, A., Hassan, M., Ellahi, R. & Nawaz, M. Shape effect of nanosize particles in unsteady mixed convection flow of nanofluid over disk with entropy generation. *Proc. Inst. Mech. Eng. E J. Process Mech. Eng.* **231**, 871–879. <https://doi.org/10.1177/0954408916646139> (2018).
- Ahmed, N., Adnan, D., Khan, U. & Mohyud-Din, S. T. Influence of shape factor on flow of magneto-nanofluid squeezed between parallel disks. *Alex. Eng. J.* <https://doi.org/10.1016/j.aej.2017.03.03> (2017).
- Haq, R. U., Noor, N. F. M. & Khan, Z. H. Numerical simulation of water based magnetite nanoparticles between two parallel disks. *Adv. Powder Technol.* **27**, 1568–1575. <https://doi.org/10.1016/j.apt.2016.05.020> (2016).
- Khan, U., Ahmed, N. & Mohyud-Din, S. T. Analysis of magnetohydrodynamic flow and heat transfer of Cu-water nanofluids between parallel plates for different shapes of nanoparticles. *Nat. Comput. Appl.* <https://doi.org/10.1177/16878140166637318> (2016).
- Hajabdollahi, H. & Hajabdollahi, Z. Numerical study on impact behavior of nanoparticle shapes on the performance improvement of shell and tube heat exchanger. *Chem. Eng. Res. Des.* **125**, 449–460. <https://doi.org/10.1016/j.cherd.2017.05.005> (2016).
- Kucherik, A. O., Arakelyan, S. M., Kutrovskaya, S. V., Osipov, A. V., Istratov, A. V., Vartanyan, T. A., & Itina, T. E. Structure and morphology effects on the optical properties of bimetallic nanoparticle films laser deposited on a glass substrate (2017), Article ID 8068560. <https://doi.org/10.1155/2017/8068560>.
- Ghozatloo, A., Maleki, S. A., Niassar, M. S. & Rashidi, A. M. Investigation of nanoparticles morphology on viscosity of nanofluids and new correlation for prediction. *JNS* **5**(2015), 161–168 (2015).
- Dogonchi, A. S., Chamkha, A. J., Seyyedi, S. M. & Ganji, D. D. Radiative nanofluid flow and heat transfer between parallel disks with penetrable and stretchable walls considering Cattaneo-Christov heat flux model. *Heat Transf.* <https://doi.org/10.1002/hjt.21339> (2018).
- Mochizuki, S. & Yang, W. J. Local heat performance and Mechanisms in radial flow between parallel disk. *J. Thermophys.* <https://doi.org/10.2514/3.13> (2012).
- Raju, N. A. & Kundu, P. K. Influence of Hall current on radiative nanofluid flow over a spinning disk: a hybrid approach. *Phys. E.* <https://doi.org/10.1016/j.physe.2019.03.006> (2019).
- Bhattacharyya, A., Seth, G. S., Kumar, R. & Chamkha, A. J. Simulation of Cattaneo-Christov heat flux on the flow of single and multi-walled carbon nanotubes between two stretchable coaxial rotating disks. *J. Therm. Anal. Calorim.* <https://doi.org/10.1007/s10973-019-08644-4> (2019).
- Bhat, A. & Katagi, N. N. Micropolar fluid flow between a non-porous disk and a porous disk with slip. *Ain Shams Eng. J.* <https://doi.org/10.1016/j.asej.2019.07.006> (2019).
- Maskeen, M. M., Zeeshan, A., Mehmood, O. U. & Hassan, M. Heat transfer enhancement in hydromagnetic alumina–copper/water hybrid nanofluid flow over a stretching cylinder. *J. Therm. Anal. Calorim.* <https://doi.org/10.1007/s10973-019-08304-7> (2019).
- Ghaffar, M., Yasmin, A. K. & Ashraf, A. Unsteady flow between two orthogonally moving porous disks. *J. Mech.* **31**, 147–151. <https://doi.org/10.1017/jmech.2014.90> (2015).
- Ahmed, N., Adnan, U. & Khan, S. T. Mohyud Din, Influence of shape factor on flow of magneto nanofluid squeezed between parallel disks. *Alex. Eng. J.* **57**, 1893–1903. <https://doi.org/10.1016/j.aej.2017.03.031> (2018).

19. Hayat, T. & Nadeem, S. Heat transfer enhancement with Ag-CuO/water hybrid nanofluid. *Results Phys.* <https://doi.org/10.1016/j.rinp.2017.06.034> (2017).
20. Hussein, A. M., Noor, M. M., Kadrigama, K., Ramasamy, D. & Rahman, M. M. Heat transfer enhancement using hybrid nanoparticles in ethylene glycol through a horizontal heated tube. *Int. J. Autom. Mech. Eng.* <https://doi.org/10.15282/ijame.14.2.2017.6.0335> (2017).
21. Suriya, A. D. & Devi, U. Numerical investigation of hydromagnetic hybrid Cu-Al₂O₃/water nanofluid flow over a permeable stretching sheet with suction. *Int. J. Nonlinear Sci. Numer. Simul.* **17**, 249–257. <https://doi.org/10.1515/ijnsns-2016-0037> (2016).
22. Sarkar, J., Ghosh, P. & Adil, A. A review on hybrid nanofluids: Recent research, development and applications. *Renew. Sustain. Energy Rev.* <https://doi.org/10.1016/j.rser.2014.11.023> (2014).
23. Sundar, L. S., Sharma, K. V., Singh, M. K. & Sousa, A. C. M. Hybrid nanofluids preparation, thermal properties, heat transfer and friction factor: a review. *Renew. Sustain. Energy Rev.* <https://doi.org/10.1016/j.rser.2016.09.108> (2016).
24. Ullah, I., Hayat, T., Alsaedi, A. & Asghar, S. Dissipative flow of hybrid nanoliquid (H₂O-aluminum alloy nanoparticles) with thermal radiation. *Phys. Scr.* <https://doi.org/10.1088/1402-4896/ab31d3> (2019).
25. Tamim, H., Dinarvand, S., Hosseini, R. & Pop, I. MHD mixed convection stagnation-point flow of a nanofluid over a vertical permeable surface: a comprehensive report of dual solutions. *Heat Mass Transf.* **50**, 639–650. <https://doi.org/10.1007/s00231-013-1264-2> (2014).
26. Alfven, H. Existence of electromagnetic-hydrodynamic waves. *Nature* **150**, 405–406 (1942).
27. Emad, A. & Pop, I. MHD flow and heat transfer over a permeable stretching/shrinking sheet in a hybrid nanofluid with a convective boundary condition. *Int. J. Numer. Methods Heat Fluid Flow* <https://doi.org/10.1108/HFF-12-2018-0794> (2019).
28. Ghadikolaei, S. S., Yassari, M., Sadeghi, H., Hosseinzadeh, K. & Ganji, D. D. Investigated the thermophysical of TiO₂-Cu/water hybrid nanofluid transport depended on the shape factor in MHD stagnation point flow. *Power Technol.* **32**, 428–438 (2017).
29. Hayat, T., Qayyum, S., Imtiaz, M. & Alsaedi, A. MHD flow and heat transfer between coaxial rotating stretchable disks in a thermally stratified medium. *PLoS ONE* **11**, e0155899. <https://doi.org/10.1371/journal.pone.0155899> (2016).
30. Rashidi, S., Dehghan, M., Ellahi, R. & Riaz, M. MTJ Abad Study of stream wise transverse magnetic fluid flow with heat transfer a round a porous obstacle. *J. Magn. Magn. Mater.* **378**, 128–137 (2015).
31. Ahmad, R., Mustafa, M., Hayat, T. & Alsaedi, A. A Numerical study of MHD nanofluid flow and heat transfer past a bidirectional exponentially stretching sheet. *J. Magn. Magn. Mater.* <https://doi.org/10.1016/j.jmmm.2016.01.038> (2016).
32. Reddy, J. V. R., Sugunamma, V., Sandeep, N. & Sulochana, C. Influence of chemical reaction, radiation and rotation on MHD nanofluid flow past a permeable flat plate in porous medium. *J. Math. Niger. Soc.* <https://doi.org/10.1016/j.jnms.2015.08.004> (2015).
33. Mliki, B., Abbassi, M. A., Omri, A. & Zeghamati, B. Effects of nanoparticles Brownian motion in a linearly/sinusoidal heated cavity with MHD natural convection in the presence of uniform heat generation/absorption. *Powder Technol.* **295**, 69–83. <https://doi.org/10.1016/j.powtec.2016.03.038> (2016).
34. Turkyilmazoglu, M. Nanofluid flow and heat transfer due to a rotating disk. *Comput. Fluids* **94**, 139–146. <https://doi.org/10.1016/j.compfluid.2014.02.009> (2014).
35. Hussain, A., Mohyud-Din, S. T. & Cheema, T. A. Analytical and numerical approaches to squeezing flow and heat transfer between two parallel disks with velocity slip and temperature jump. *Chin. Phys. Lett.* **29**, 114705. <https://doi.org/10.1088/0256-307x/29/11/114705> (2012).
36. Vajravelu, K., Prasad, K. V., Chiu, O. & Vaidya, H. MHD squeeze flow and heat transfer of a nanofluid between parallel disks with variable fluid properties and transpiration. *Mater. Eng.* <https://doi.org/10.1186/s40712-017-0076-4> (2017).
37. Chamkha, A. J., Dogonchi, A. S. & Ganji, D. D. Magneto-hydrodynamic flow and heat transfer of a hybrid nanofluid in a rotating system among two surfaces in the presence of thermal radiation and Joule heating. *AIP Adv.* **9**, 025103. <https://doi.org/10.1063/1.5086247> (2019).
38. Waini, A., Ishak, D. & Pop, I. MHD flow and heat transfer of a hybrid nanofluid past a permeable stretching/shrinking wedge. *Appl. Math. Mech. Engl. Ed.* **41**, 507–520. <https://doi.org/10.1007/s10483-020-2584-7> (2019).
39. Hashmi, M. M., Hayat, T. & Alsaedi, A. On the analytic solutions for squeezing flow of nanofluid between parallel disks. *Nonlinear Anal. Model Control* **17**, 418–430 (2012).
40. Sheikholeslami, M. & Jafaryar, M. Nanoparticles for improving the efficiency of heat recovery unit involving entropy generation analysis. *J. Taiwan Inst. Chem. Eng.* <https://doi.org/10.1016/j.jtice.2020.09.033> (2020).
41. Wang, G., Yao, Y., Chen, Z. & Hu, P. Thermodynamic and optical analyses of a hybrid solar CPV/T system with high solar concentrating uniformity based on spectral beam splitting technology. *Energy* **166**, 256–266 (2019).
42. Guo, C. *et al.* Structural hybridization of bimetallic zeolitic imidazolate framework (ZIF) nanosheets and carbon nanofibers for efficiently sensing α -synuclein oligomers. *Sens. Actuators B Chem.* <https://doi.org/10.1016/j.snb.2020.127821> (2020).
43. Yan, H. *et al.* Reversible Na⁺ insertion/extraction in conductive polypyrrole-decorated NaTi₂(PO₄)₃ nanocomposite with outstanding electrochemical property. *Appl. Surf. Sci.* **530**, 47295. <https://doi.org/10.1016/j.apsusc.2020.147295> (2020).
44. Sheikholeslami, M. & Farshad, S. A. Investigation of solar collector system with turbulator considering hybrid nanoparticles. *Renew. Energy* **171**, 1128–1158 (2021).
45. Sheikholeslami, M., Farshad, S. A., Ebrahimpour, Z. & Said, Z. Recent progress on flat plate solar collectors and photovoltaic systems in the presence of nanofluid: a review. *J. Clean. Prod.* **293**, 126119 (2021).
46. Kashif, A., Akbar, M. Z., Iqbal, M. F. & Ashraf, M. Numerical simulation of heat and mass transfer in unsteady nanofluid between two orthogonally moving porous coaxial disks. *AIP Adv.* **4**, 107113. <https://doi.org/10.1063/1.4897947> (2014).
47. Huanan, Y. *et al.* The NO_x degradation performance of nano-TiO₂ coating for asphalt pavement. *Nanomaterials* **10**(2020), 897. <https://doi.org/10.3390/nano10050897> (2020).
48. Yousefi, M., Dinarvand, S., Yazdi, E. & Pop, I. Stagnation-point flow of an aqueous titania-copper hybrid nanofluid toward a wavy cylinder. *Int. J. Numer. Methods Heat Fluid Flow* <https://doi.org/10.1108/HFF-01-2018-000e> (2018).
49. Rostami, N., Dinarvand, S. & Pop, I. Dual solutions for mixed convective stagnation-point flow of an aqueous silica-alumina hybrid nanofluid. *Chin. J. Phys.* **56**, 2465–2478. <https://doi.org/10.1016/j.cjph.2018.06.013> (2018).
50. Majdalani, J., Zhou, C. & Dawson, C. A. Two dimensional viscous flows between slowly expanding or contracting walls with weak permeability. *J. Biomech.* **35**, 1399–1403 (2015).

Acknowledgements

The authors extend their appreciation to the Deanship of Scientific Research at King Khalid University, Abha 61413, Saudi Arabia for funding this work through research groups program under Grant Number R.G.P-2-13/42. The authors are grateful to the Deanship of Scientific Research, King Saud University for funding through Vice Deanship of Scientific Research Chairs.

Author contributions

M.Z.A. and S.B. conceived the study. M.Z.A. and Q.R. carried out the calculations. M.Z.A., S.B., and Q.R. analyzed the results. M.Z.A. wrote the manuscript. M.Y. Malik: He has assisted to authors present before revision

regarding the incorporation of suggestions made by reviewers. He has provided references to mathematical modeling and numerical results. E.M. Sherif: Physical description of graphical results is explained more clearly by the added author along with a resolution of figures. Yong-Min Li: He has removed punctuation errors along with sentence structuring mistakes and done proofread the complete manuscript. Overall, all authors participate to improve the quality of the manuscript.

Competing interests

The authors declare no competing interests.

Additional information

Correspondence and requests for materials should be addressed to M.Z.A.Q. or Y.-M.L.

Reprints and permissions information is available at www.nature.com/reprints.

Publisher's note Springer Nature remains neutral with regard to jurisdictional claims in published maps and institutional affiliations.



Open Access This article is licensed under a Creative Commons Attribution 4.0 International License, which permits use, sharing, adaptation, distribution and reproduction in any medium or format, as long as you give appropriate credit to the original author(s) and the source, provide a link to the Creative Commons licence, and indicate if changes were made. The images or other third party material in this article are included in the article's Creative Commons licence, unless indicated otherwise in a credit line to the material. If material is not included in the article's Creative Commons licence and your intended use is not permitted by statutory regulation or exceeds the permitted use, you will need to obtain permission directly from the copyright holder. To view a copy of this licence, visit <http://creativecommons.org/licenses/by/4.0/>.

© The Author(s) 2021